PAPER • OPEN ACCESS

Wafer-scale graphene quality assessment using micro four-point probe mapping

View the article online for updates and enhancements.

IOP ebooks™

Bringing together innovative digital publishing with leading authors from the global scientific community.

Start exploring the collection−download the first chapter of every title for free.

Wafer-scale graphene quality assessment using micro four-point probe mapping

David M A Mackenzie[1,2,8] ⓘ **, Kristoffer G Kalhauge**[1,3] ⓘ **,**
Patrick R Whelan[1,3] ⓘ **, Frederik W Østergaard**[4]**, Iwona Pasternak**[5,6]**,**
Wlodek Strupinski[5,6]**, Peter Bøggild**[1,3] ⓘ **, Peter U Jepsen**[7] **and**
Dirch H Petersen[1,3] ⓘ

[1] Center for Nanostructured Graphene (CNG), Technical University of Denmark, DK-2800, Kgs. Lyngby, Denmark
[2] Department of Electronics and Nanoengineering, Aalto University, PO Box 13500, FI-00076 Aalto, Finland
[3] Department of Physics, Technical University of Denmark, DK-2800, Kgs. Lyngby, Denmark
[4] CAPRES—A KLA Company, Scion-DTU, Bld. 373, DK-2800, Kgs. Lyngby, Denmark
[5] Faculty of Physics, Warsaw University of Technology, Koszykowa 75, 00-662 Warsaw, Poland
[6] ENT SA, Szucha 8, 00-582 Warsaw, Poland
[7] Department of Photonic Engineering, Technical University of Denmark, DK-2800, Kgs.Lyngby, Denmark

E-mail: david.mackenzie@aalto.fi and dhpe@dtu.dk

CrossMark

Abstract

Micro four-point probes (M4PP) provide rapid and automated lithography-free transport properties of planar surfaces including two-dimensional materials. We perform sheet conductance wafer maps of graphene directly grown on a 100 mm diameter SiC wafer using a multiplexed seven-point probe with minor additional measurement time compared to a four-point probe. Comparing the results of three subprobes we find that compared to a single-probe result, our measurement yield increases from 72%–84% to 97%. The additional data allows for correlation analysis between adjacent subprobes, that must measure the same values in case the sample is uniform on the scale of the electrode pitch. We observe that the relative difference in measured sheet conductance between two adjacent subprobes increase in the transition between large and low conductance regions. We mapped sheet conductance of graphene as it changed over several weeks. Terahertz time-domain spectroscopy conductivity maps both before and after M4PP mapping showed no significant change due to M4PP measurement, with both methods showing the same qualitative changes over time.

Supplementary material for this article is available online

Keywords: graphene, SiC, conductance, micro four-point probe, terahertz spectroscopy, metrology, mapping

(Some figures may appear in colour only in the online journal)

[8] Author to whom any correspondence should be addressed.

1. Introduction

Graphene is an atomically-thin two-dimensional material [1–3] which has properties suitable for a large number of practical technologies from corrosion protection [4–6] to OLEDS [7–9] to sensors [10–12]. Now that the capability of large-scale growth [13–15], transfer [16–18], and lithography techniques [19, 20] of

1

graphene are well established, methods for assessing the quality [21, 22] and homogeneity of wafer-scale graphene are required to mature graphene-based technologies. Despite these advances in growth and processing, graphene inhomogeneity remains an issue for large-scale graphene. Areas of bilayer graphene are very difficult to eliminate and affect device properties [23–25]. In addition, significant variations in sheet conductance and carrier density are challenging to eliminate on large scale [18, 26–28]. Finding accurate strategies to probe thin-film properties is important for future research into the optimisation and commercialisation of graphene. Ideally, these methods should not require any wafer dicing (so the characterized wafer can be further processed), or contact with liquids or polymers so to not change the properties of the material [29]. Several techniques can probe thin-film properties without lithography.

1.1. Micro-Raman spectroscopy

Due to extensive work on the Raman spectral response of graphite and carbon nanotubes [30] prior to the graphene research boom, micro-Raman analysis was a tool that fit easily into the toolbox of the early graphene researcher. Therefore micro-Raman spectroscopy has become one of the key technologies used in the characterization of graphene because it is able to imply many metrics of graphene quality, including, but not limited to, number of layers [31, 32], defect density [33, 34], strain [35, 36], and doping [37, 38].

The resolution of micro-Raman depends on the laser wavelength and objective, full width at half maximum is typically <1 μm. Although micro-Raman is useful for graphene characterisation the technique cannot obtain direct measurement of sheet conductance (G_S).

1.2. Terahertz time-domain spectroscopy

Terahertz time-domain spectroscopy (THz-TDS) is a non-contact method where a THz pulse attenuated by graphene is translated into G_S [39, 40]. Graphene G_S measurements can be performed in either transmission-mode [41] or reflection-mode [42]. The beam spot diameter of a 1 THz pulse is ≈ 1 mm, however, for typical graphene the mean free path for one pulse is ≈ 10 nm [21]. This results in each THz pixel being the average of ≈ 10 nm transport properties in an mm-sized area. The probed area must be several millimetres away from metal contacts/contamination, as the large number of carriers can significantly affect the THz signal [43]. THz-TDS can also extract G_S for graphene on polymer [44] and has been used for tracking graphene properties before and after processing [43, 45].

1.3. Micro four-point probes

Micro four-point probes (M4PPs) consist of micron-sized metal-coated cantilevers that are attached to a silicon carrier [46]. The electrodes are brought into contact with the sample using a strain gauge sensor to detect the surface [47]. G_S is then measured using lock-in technique applying dual configuration van der Pauw type correction [48]. G_S measured with M4PPs typically have errors less than 0.1% [49] even when measuring in confined regions on a scale similar to the probe size [50]. Hall

measurements are also possible [51] as well as determination if current flows in a 1D or 2D path [28, 52, 53]. The resolution and probing area of M4PPs is on the order of the probe pitch ≈ 10 μm. Fully automated M4PP systems are commercially available and are typically used for G_S characterisation of metallic and semiconductor thin films [54].

1.4. G_S mapping of graphene

The discussed methods can all be used to generate high resolution spatial *maps* of graphene properties. Micro-Raman cannot probe G_S, and there are several differences between G_S maps obtained via THz-TDS and M4PP. M4PP has higher spatial resolution (≈ 10 μm versus $\approx$mm) whereas THz-TDS probes on the order of 10 nm versus 10 μm for M4PP. The differences in mean-free path could lead to different results if graphene has grain boundaries between 10 nm and 10 μm, which should be considered when choosing a mapping method or performing analysis. Transmission-mode THz-TDS has specific wafer requirements: the substrate should be flat on both sides and be (near) transparent in the THz range. Reflection-mode THz-TDS does not require a specialized THz-transparent wafer, but has a lower tolerance for alignment error. M4PP does not have any specific wafer requirements other than a substrate that is less conducting than the thin film to be measured. But M4PP requires probes to be in direct contact with graphene.

Previously we have analyzed a 100 mm diameter graphene-coated SiC wafer using G_S maps obtained via THz-TDS and a single-probe M4PP [28] in order to examine wafer-scale variations. During this study a potential weakness of the M4PP method became apparent, dead pixels could occur because of failed contact for an individual probe engage (all four electrodes are required to be in good electrical contact for any measurement to be performed) or due to probe failure typically after few thousands measurements. In order to make the M4PP technique more robust we repeated the measurements with an equidistant seven-point probe, enabling us to significantly increase measurement yield, as well as provide novel homogeneity information that can be applied to thin film analysis in general.

2. Methods

Graphene was grown on a four-inch silicon carbide wafer as described previously [28, 55]. Electrical measurements were performed with a CAPRES microRSP-A300 using lock-in technique at 12 Hz, and with a current of 250 μA. In this work we have used a probe with seven nickel-coated electrodes as shown in figure 1(a), which are based on three-way flexible electrodes [56, 57] to minimize lateral forces. The right-hand-side of figure 1(a) shows a strain gauge, which is used to control the contact force when the probe is engaged on the surface [47]. A low contact force and three-way flexible electrodes [56, 57] are used to prevent unnecessary damage to the probe and surface. During a single engage of the probe to the surface, electrical measurements were performed in A-configuration, and then B-configuration as
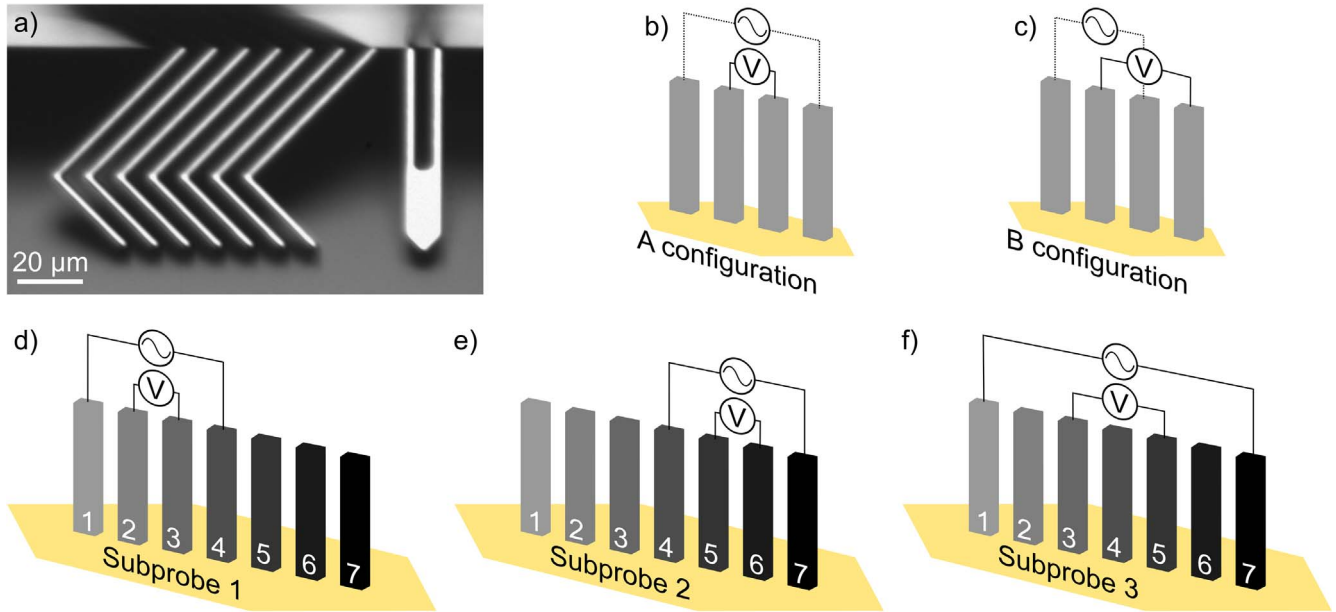
Figure 1. M4PP configurations and subprobes. (a) Optical microscope image of the l-shaped cantilever-based seven-point-probe used for measurements equipped with strain gauge. (b)–(c) Measurement configurations A and B. (d) Subprobe 1 with 10 μm pitch. (e) Subprobe 2 with 10 μm pitch. (f) Subprobe 3 with 20 μm pitch.

defined in figures 1(b)–(c), respectively. With seven electrodes available, we can select four electrodes of the seven to create a *subprobe*. The three subprobes used in this paper are shown in figures 1(d)–(f), where subprobes 1 and 2 have 10 μm electrode pitch and subprobe 3 has 20 μm electrode pitch. Subprobes 1 and 2 were chosen since they are the smallest possible subprobes with the least overlap. Subprobe 3 is the largest possible subprobe. Each engage involves movement of the probe to the new measurement position, surface approach, and measurement. Based on 24 measurements and 400 μm pixel-pitch our measurement time per pixel is 7 s.

During each engage a total of 24 resistance measurements were performed (8 for each subprobe). These multiplexed measurements enabled a variety of error-checking measures to increase result accuracy as previously described [58]. Firstly, because the measurements were performed with lock-in technique, the phase of each individual measurement was assessed, and individual resistance measurements rejected if outside a set tolerance. The sheet resistance (R_S) is determined from the modified van der Pauw equation [48, 50] using resistance values measured in *A* configuration (R_A) and *B* configuration (R_B)

$$e^{\frac{2\pi R_A}{R_s}} - e^{\frac{2\pi R_B}{R_s}} = 1.$$

All accepted sheet resistance values were then subjected to a median filter and the mean of the remaining sheet resistance values $\langle R_S \rangle$ which pass the filter gave a single sheet conductance $G_S = \langle R_S^{-1} \rangle$ value for the subprobe. If no $\langle R_S \rangle$ values pass the filters with the set tolerances, then we define the sheet conductance $G_S = 0$ in subsequent analysis and mapping. Probes were replaced automatically every 2000 engages from the M4PP probe cassettes loaded in the microRSP-A300. In order to combine the three subprobe maps (figures 2(a)–(c)) to the combined map (figure 2(d)), each pixel G_S values from all subprobes that had previously passed the median filter, were combined

using an additional median filter. The median of the remaining values is used for the combined subprobe map. In this work our phase tolerance was 1°, and all median filter tolerances were 2%.

3. Results and discussion

Wafer-scale G_S maps performed with each of the three subprobes are shown in figures 2(a)–(c) with a map combining the data from all three subprobes is shown in figure 2(d). Previously, M4PP data from this wafer was compared with a THz-TDS conductance map [28]. Here, we compare G_S results obtained from different subprobes during the same probe engage. For a perfectly uniform material using multiple subprobes provides a redundancy in the measurement, in case of subprobe failure or localized sample defects. In either case, a measurement from one of the other subprobes may be successful.

Qualitatively, all the subprobe maps in figures 2(a)–(c) are similar, each having different regions where no G_S values passed the filters described in the methods section. The most prominent of these features appear as annulus sectors (circular ring sectors) and are attributed to subprobe failure as it matches the spiral-like measurement order. Thus, there is no reason to attribute these measurement failures to the local thin-film properties.

When G_S from the three subprobes are combined (figure 2(d)) all the null-G_S annulus sectors disappear. We then find that for this combined map only 385 out of 11 310 engages did not return an accepted G_S value (10 925 accepted, 97%). In contrast, the successful measurements for individual subprobes was 9528 (84% accepted), 9135 (81% accepted) and 8163 (72% accepted), for subprobe 1, subprobe 2, subprobe 3, respectively. For our measurements choosing more than one subprobe offered a level of measurement redundancy, with significant higher measurement yield from
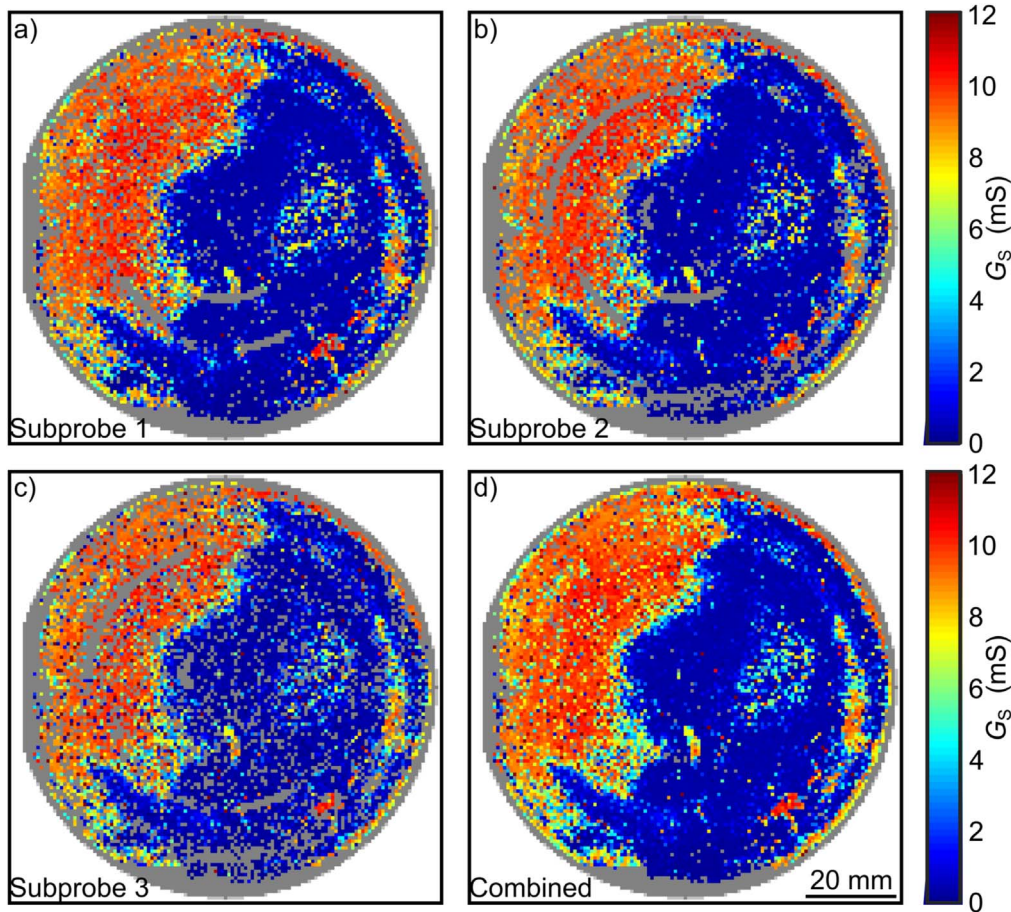
Figure 2. Conductance maps measured with M4PP. (a) Subprobe 1 (10 μm pitch). (b) Subprobe 2 (10 μm pitch). (c) Subprobe 3 (20 μm pitch). (d) Combination of data from subprobes from (a) to (c). Dead pixels/wafer outline shown in grey.

72%–84% to 97%. Although some regions of the wafer have over an order of magnitude lower G_S, by studying the R_A/R_B ratio of the measurements (figure S1 is available online at stacks.iop.org/NANO/31/225709/mmedia), it can be concluded that this graphene does not exhibit any significant quasi 1D electrical behaviour.

Increasing the number of subprobes also increases the total measurement time. The time to measure one subprobe, disengage, move and reengage took approximately five seconds. Measurement time was increased by one second per additional subprobe. Three subprobes were chosen as a good compromise between measurement yield and measurement time. For a non-uniform sample, multiple subprobe analysis can reveal the spatial and quantitative information about the extent of inhomogeneities.

Multi-subprobe G_S maps can be a useful metrology tool for evaluating the variation in thin film/2D material quality across a wafer. With a wafer map of G_S enough data is available to perform analysis that would otherwise be impossible or imprecise with a linescan, reduced-area map, or single probe scan. For example, a comparison between G_S values for different subprobes can be compared to give an insight into homogeneity on the order of the probe length. Figure 3(a) shows a uniformity map of figure 2(d), which was calculated using the relative standard deviation of each pixel and its 15

nearest neighbours (uniformity maps for different number of nearest neighbours are shown in figure S2). The single-subprobe uniformity maps for data from figures 2(a)–(c) are shown in figures S3(a)–(c), where the lack of data coverage conceals many uniformity features. Homogeneity is known to be important for two-dimensional device performance [59, 60], so it is important to know if the entire wafer, or certain areas are suitable for device processing.

The subprobe-to-subprobe conductance correlation is shown in figure 3(b), where four regions are defined: $G_S < 0.3$ mS (black region), 0.3 mS $\leqslant G_S < 0.75$ mS (blue region), 0.75 mS $\leqslant G_S < 7.5$ (green region), 7.5 mS $\leqslant G_S$ (red region). We observe good subprobe-to-subprobe agreement for high and low values of G_S, the blue and red regions, but poorer agreement in the green region. The fact the subprobe-to-subprobe error decreases again for the red region shows the subprobe-subprobe error is not simply proportional to the magnitude of G_S, and is likely an indication the green region has variations on the order of the probe length, a result which is in good agreement with previous analysis [28]. When figure 2(b) is replotted using the colourscale from figure 3(b), we in fact do observe most of the green pixels as a transition area separating the regions of high and low values of G_S. Because the width of the transition areas are
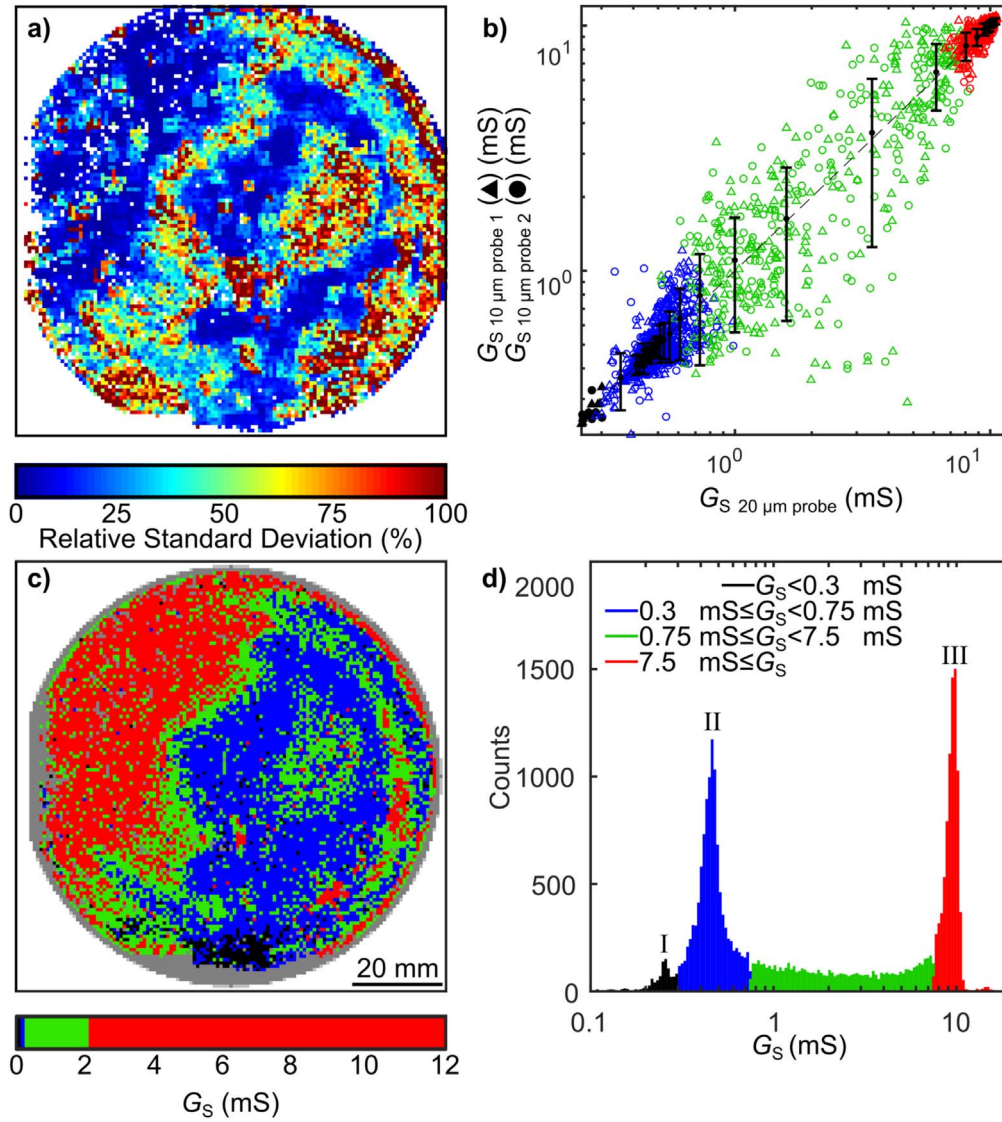
Figure 3. (a) Uniformity map of data from figure 2(d) showing the relative standard deviation of 24 nearest neighbours. (b) Subprobe-to-subprobe correlation comparing subprobe 3 with subprobe 1 (triangles) and subprobe 2 (circles). Four regions of G_S are defined by $G_S < 0.3$ mS (black region), 0.3 mS $\leqslant G_S < 0.75$ mS (blue region), 0.75 mS $\leqslant G_S < 7.5$ (green region), 7.5 mS $\leqslant G_S$ (red region). (c) Figure 2(d) replotted in colourscale from figure 3(b). (d) Histogram of the conductance as measured by all three subprobes with three peaks in the data I–III.

significantly larger than the size of the probe, it can be concluded this data represents a true variation in the sample G_S.

When the G_S data for all subprobes is plotted as a histogram three distinct peaks emerge, as shown in figure 3(c), where the peaks are labelled I through III, and in addition between peak II and peak III a plateau in the data where the counts are roughly constant. Measurements representing the three peaks all originate from connected regions of graphene. The plateau between the second and third peak originates from measurements made in the transition area. Representing the data as a histogram allows for easy comparison of changes to the wafer over time.

G_S was also mapped at different times over several weeks using THz-TDS and M4PP, expanding on the work from [28]. After the maps shown above, a THz-TDS map of the wafer was performed, followed by an additional M4PP map, and

then by a second THz-TDS map. Damage to graphene is easily detected by THz-TDS, for example damage attributed to mishandling by using a wafer tweezer is visible when comparing figure S4b and figure S4d, with the damage features matching the dimensions of the tweezer tines. Histogram analysis of the THz-TDS/M4PP maps are shown in figure S5 and show that the two THz-TDS maps are almost identical, suggesting that the intervening M4PP map has not made significant changes the sample. These repeated maps suggest that the contact forces used to directly probe of graphene with an M4PP is very well controlled by the strain gauge and microRSP-A300 hardware and lead to no significant graphene damage.

Overall, we observe slightly higher G_S values in the M4PP map in comparison to both THz-TDS results, which is expected due to the fact that M4PP analyses G_S over

micron-sized areas whereas THz-TDS at 1 THz probes over tens of nanometres [21]. We also note that peak I and II observed in figure 3(d) have now combined as part of the change in G_S over time. The progression of wafer changes over nine weeks are shown in figure S4. The changes over time are quantitatively similar for both M4PP and THz-TDS showing that either method has the resolution required to track changes in graphene over time.

We have the following recommendations when G_S mapping graphene. THz-TDS and M4PP both provide information about graphene uniformity. Both methods deliver equivalent results in some cases- for uniform graphene where the G_S on the few-nm scale matches that on the μm scale. THz-TDS is faster, non-contact and performs well on uniform samples. However, when device processing requires G_S knowledge on the order of microns to millimetres, then M4PP mapping is still preferred. If metal is present near test regions M4PP mapping is more reliable than THz-TDS. Beyond graphene, 2D materials/thin films of various THz opacities are possible to map with a M4PP system. Generally, choosing to use a M4PP with more than four electrodes allows for additional subprobe measurements while adding negligible additional measurement time. This also allows a level of measurement redundancy for failed measurements, and allows insightful additional analysis. We have shown in figure 2 that a higher accuracy G_S, with fewer dead pixels was achieved by combining the data from subprobes into a single map. In addition, the combined map can be used via both uniformity assessment (e.g. Figure 3(a)) and subprobe-correlational assessment of G_S to determine spatial quality. The technique is sensitive enough to track changes in the graphene over time.

4. Conclusion

In summary, we have investigated wafer conductance maps of graphene using multiple subprobe M4PPs. Combining subprobes increased measurement yield from under 85% to 97% without adding significant measurement time. G_S varied across the wafer by over an order of magnitude, leading to local regions with different G_S landscapes. Producing wafer-scale analysis can be used to determine overall growth quality, identify graphene areas which are suitable for further device processing, or to reject/accept an entire wafer and such analysis can be performed for M4PP maps of other materials. The M4PP map was compared to THz-TDS which showed qualitatively similar maps, even when the wafer changed over many weeks, further suggesting that M4PP produces accurate G_S data. THz-TDS conductivity maps performed before and after the M4PP mapping showed no decrease in conductivity attributable to the M4PP process.

Acknowledgments

ORCID iDs

David M A Mackenzie https://orcid.org/0000-0003-1114-2955
Kristoffer G Kalhauge https://orcid.org/0000-0002-9896-6289
Patrick R Whelan https://orcid.org/0000-0002-3978-7029
Peter Bøggild https://orcid.org/0000-0002-4342-0449
Dirch H Petersen https://orcid.org/0000-0002-9309-4186

References

[1] Novoselov K S *et al* 2005 Two-dimensional gas of massless Dirac fermions in graphene *Nature* **438** 197–200
[2] Novoselov K S 2011 Nobel lecture: graphene: materials in the flatland *Rev. Mod. Phys.* **83** 837–49
[3] Blake P *et al* 2007 Making graphene visible *Appl. Phys. Lett.* **91** 063124
[4] Yu F *et al* 2018 Complete long-term corrosion protection with chemical vapor deposited graphene *Carbon* **132** 78–84
[5] Kirkland N T, Schiller T, Medhekar N and Birbilis N 2012 Exploring graphene as a corrosion protection barrier *Corros. Sci.* **56** 1–4
[6] Galbiati M, Stoot A C, Mackenzie D M A, Bøggild P and Camilli L 2017 Real-time oxide evolution of copper protected by graphene and boron nitride barriers *Sci. Rep.* **7** 1–7
[7] Han T-H *et al* 2012 Extremely efficient flexible organic light-emitting diodes with modified graphene anode *Nat. Photon.* **6** 105–10
[8] Wu J *et al* 2010 Organic light-emitting diodes on solution-processed graphene transparent electrodes *ACS Nano* **4** 43–8
[9] Sun T *et al* 2010 Multilayered graphene used as anode of organic light emitting devices *Appl. Phys. Lett.* **96** 133301
[10] Cagliani A, Mackenzie D M A, Tschammer L K, Pizzocchero F, Almdal K and Bøggild P 2014 Large-area nanopatterned graphene for ultrasensitive gas sensing *Nano Res.* **7** 743–54
[11] Yoon H J, Jun D H, Yang J H, Zhou Z, Yang S S and Cheng M M C 2011 Carbon dioxide gas sensor using a graphene sheet *Sensors Actuators* B **157** 310–3
[12] Gopalan K K *et al* 2018 Scalable and tunable periodic graphene nanohole arrays for mid- infrared plasmonics *Nano Lett.* **18** 5913–8
[13] Luo B *et al* 2017 Sputtering an exterior metal coating on copper enclosure for large-scale growth of single-crystalline graphene *2D Mater.* **4** 045017
[14] Miseikis V *et al* 2015 Rapid CVD growth of millimetre-sized single crystal graphene using a cold-wall reactor *2D Mater.* **2** 014006
[15] Kim K S *et al* 2009 Large-scale pattern growth of graphene films for stretchable transparent electrodes *Nature* **457** 706–10
[16] Shivayogimath A *et al* 2019 Do-it-yourself transfer of large-area graphene using an office laminator and water *Chem. Mater.* **31** 2328–36

[17] Whelan P R *et al* 2017 Raman spectral indicators of catalyst decoupling for transfer of CVD grown 2D materials *Carbon* **117** 75–81

[18] Shivayogimath A *et al* 2019 Atomic layer deposition alumina-mediated graphene transfer for reduced process contamination *Phys. Status Solidi* **13** 1900424

[19] Mackenzie D M A *et al* 2017 Batch fabrication of nanopatterned graphene devices via nanoimprint lithography *Appl. Phys. Lett.* **111** 193103

[20] Mackenzie D M A *et al* 2015 Fabrication of CVD graphene-based devices via laser ablation for wafer-scale characterization *2D Mater.* **2** 045003

[21] Bøggild P *et al* 2017 Mapping the electrical properties of large-area graphene *2D Mater.* **4** 042003

[22] Jessen B S *et al* 2018 Quantitative optical mapping of two-dimensional materials *Sci. Rep.* **8** 6381

[23] Yakimova R *et al* 2014 Morphological and electronic properties of epitaxial graphene on SiC *Physica* B **439** 54–9

[24] Panchal V, Giusca C E, Lartsev A, Yakimova R and Kazakova O 2014 Local electric field screening in bi-layer graphene devices *Front. Phys.* **2** 3

[25] Mackenzie D M A, Panchal V, Petersen D H and Kazakova O 2019 Qualitative analysis of scanning gate microscopy on epitaxial graphene *2D Mater.* **6** 025023

[26] Bloos D *et al* 2019 Contactless millimeter wave method for quality assessment of large area graphene *2D Mater.* **6** 035028

[27] Deng B, Liu Z and Peng H 2019 Toward mass production of CVD Graphene films *Adv. Mater.* **31** 1–25

[28] Whelan P R *et al* 2018 Electrical homogeneity mapping of epitaxial graphene on silicon carbide *ACS Appl. Mater. Interfaces* **10** 31641–7

[29] Gammelgaard L *et al* 2014 Graphene transport properties upon exposure to PMMA processing and heat treatments *2D Mater.* **1** 035005

[30] Ferrari A C and Robertson J 2000 Interpretation of Raman spectra of disordred and amorphous carbon *Phys. Rev.* B **61** 14295

[31] Ferrari A C *et al* 2006 Raman spectrum of graphene and graphene layers *Phys. Rev. Lett.* **97** 1–4

[32] Malard L M, Pimenta M A, Dresselhaus G and Dresselhaus M S 2009 Raman spectroscopy in graphene *Phys. Rep.* **473** 51–87

[33] Cançado L G *et al* 2011 Quantifying defects in graphene via raman spectroscopy at different excitation energies *Nano Lett.* **11** 3190–6

[34] Chen J H, Cullen W G, Jang C, Fuhrer M S and Williams E D 2009 Defect scattering in graphene *Phys. Rev. Lett.* **102** 1–4

[35] Neumann C *et al* 2015 Raman spectroscopy as probe of nanometre-scale strain variations in graphene *Nat. Commun.* **6** 1–7

[36] Larsen M B B S, Mackenzie D M A, Caridad J M, Bøggild P and Booth T J 2014 Transfer induced compressive strain in graphene: evidence from Raman spectroscopic mapping *Microelectron. Eng.* **121** 113–7

[37] Kim D C, Jeon D Y, Chung H J, Woo Y, Shin J K and Seo S 2009 The structural and electrical evolution of graphene by oxygen plasma-induced disorder *Nanotechnology* **20** 375703

[38] Lee J E, Ahn G, Shim J, Lee Y S and Ryu S 2012 Optical separation of mechanical strain from charge doping in graphene *Nat. Commun.* **3** 1024–8

[39] Christian Due J, Uhd P and Jepsen P U 2013 *Terahertz transport dynamics of graphene charge carriers* Technical University of Denmark (https://orbit.dtu.dk/files/87595900/JBuronThesis_Final_printFormat.pdf)

[40] Buron J D *et al* 2015 Graphene mobility mapping *Sci. Rep.* **5** 12305

[41] Buron J D *et al* 2012 Graphene conductance uniformity mapping *Nano Lett.* **12** 5074–81

[42] Mackenzie D M A *et al* 2018 Quality assessment of terahertz time-domain spectroscopy transmission and reflection modes for graphene conductivity mapping *Opt. Express* **26** 9220–9

[43] Mackenzie D M A, Buron J D, Boaggild P, Jepsen P U and Petersen D H 2016 Contactless graphene conductance measurements: the effect of device fabrication on terahertz time-domain spectroscopy *Int. J. Nanotechnol.* **13** 591–6

[44] Whelan P R *et al* 2018 Conductivity mapping of graphene on polymeric films by terahertz time-domain spectroscopy *Opt. Express* **26** 17748–54

[45] Gopalan K K *et al* 2018 Scalable and tunable periodic graphene nanohole arrays for mid-infrared plasmonics *Nano Lett.* **18** 5913–8

[46] Petersen C L, Grey F, Shiraki I and Hasegawa S 2000 Microfour-point probe for studying electronic transport through surface states *Appl. Phys. Lett.* **77** 3782–4

[47] Petersen D H *et al* 2010 Review of electrical characterization of ultra-shallow junctions with micro four-point probes *J. Vac. Sci. Technol.* B **28** C1C27–1C33

[48] Rymaszewski R 1969 Relationship between the correction factor of the four-point probe value and the selection of potential and current electrodes *J. Phys. E: Sci. Instrum.* **2** 170–4

[49] Kjaer D *et al* 2008 Micro four-point probe with high spatial resolution for ion implantation and ultra-shallow junction characterization *AIP Conf. Proc.* **1066** 167–70

[50] Thorsteinsson S *et al* 2009 Accurate microfour-point probe sheet resistance measurements on small samples *Rev. Sci. Instrum.* **80** 053902

[51] Petersen D H, Hansen O, Lin R and Nielsen P F 2008 Micro-four-point probe Hall effect measurement method *J. Appl. Phys.* **104** 013710

[52] Buron J D *et al* 2014 Electrically continuous graphene from single crystal copper verified by terahertz conductance spectroscopy and micro four-point probe *Nano Lett.* **14** 6348–55

[53] Boll M *et al* 2014 Sensitivity analysis explains quasi-one-dimensional current transport in two-dimensional materials,' *Phys. Rev.* B **90** 1–5

[54] Nielsen P F *et al* 2012 Microprobe metrology for direct sheet resistance and mobility characterization *IWJT 2012: 12th Int. Work. Junction Technol.* pp 1–6

[55] Strupinski W *et al* 2011 Graphene epitaxy by chemical vapor deposition on SiC *Nano Lett.* **11** 1786–91

[56] Wang F *et al* 2011 Three-way flexible cantilever probes for static contact *J. Micromech. Microeng.* **21** 085003

[57] Kalhauge K G, Henrichsen H H and Wang F 2018 Vibration tolerance of micro-electrodes *J. Micromech. Microeng.* **28** 095010

[58] Petersen D H 2009 *Micro four-point probe and micro hall effect—methods for reliable electrical characterization of ultra-shallow junctions* Technical University of Denmark (https://orbit.dtu.dk/files/7831934/Dirch_Hjorth_Petersen_phdthesis_2009.pd)

[59] Mackenzie D M A *et al* 2017 Quality assessment of graphene: continuity, uniformity, and accuracy of mobility measurements *Nano Res.* **10** 3596–605

[60] Kaushik N *et al* 2017 Reversible hysteresis inversion in MoS$_2$ field effect transistors *npj 2D Mater. Appl.* **1** 34